

SERENDIPITOUS DISCOVERY OF AN INFRARED BOW SHOCK NEAR PSR J1549-4848 WITH *SPITZER*

ZHONGXIANG WANG¹, DAVID L. KAPLAN², PATRICK SLANE³, NIDIA MORRELL⁴, AND VICTORIA M. KASPI⁵
Draft version October 8, 2018

ABSTRACT

We report on the discovery of an infrared cometary nebula around PSR J1549–4848 in our *Spitzer* survey of a few middle-aged radio pulsars. Following the discovery, multi-wavelength imaging and spectroscopic observations of the nebula were carried out. We detected the nebula in *Spitzer* IRAC 8.0, MIPS 24 and 70 μm imaging and in *Spitzer* IRS 7.5–14.4 μm spectroscopic observations, and also in the WISE all-sky survey at 12 and 22 μm . These data were analyzed in detail, and we find that the nebula can be described with a standard bow-shock shape, and that its spectrum contains polycyclic aromatic hydrocarbon and H₂ emission features. However, it is not certain which object drives the nebula. We analyze the field stars and conclude that none of them can be the associated object because stars with a strong wind or mass ejection that usually produce bow shocks are much brighter than the field stars. The pulsar is approximately 15'' away from the region in which the associated object is expected to be located. In order to resolve the discrepancy, we suggest that a highly collimated wind could be emitted from the pulsar and produce the bow shock. X-ray imaging to detect the interaction of the wind with the ambient medium and high-spatial resolution radio imaging to determine the proper motion of the pulsar should be carried out, which will help verify the association of the pulsar with the bow shock nebula.

Subject headings: infrared: ISM — ISM: structure — stars: individual (PSR J1549–4848) — stars: neutron

1. INTRODUCTION

Interstellar shocks are seen in association with various astrophysical objects, from wind-blowing massive stars (van Buren et al. 1990), mass-ejecting giant stars (e.g., Martin et al. 2007), expanding supernova remnants (SNRs; e.g., Morton et al. 2007), to energetic pulsars (Gaensler & Slane 2006). In these objects, fast moving ejecta collide with the surrounding interstellar medium (ISM), and the strong interaction drives a shock front. Depending on the kinetic energy carried into the shock and local ISM conditions, the postshock hot material can be bright at different wavelengths. Observations of shocks not only help study shock physics, but also provide probes of the associated objects and ISM.

Depending on temperature T , the sound speed c_s in the ISM [$c_s \simeq 10(T/10^4 \text{ K})^{1/2} \text{ km s}^{-1}$] is in the range of 1–100 km s^{-1} . As a result, when stellar objects have high space velocities V_* , they can be moving supersonically in the ISM. In such cases, a shock will appear as a cometary structure (so-called bow shock), as interstellar material is swept up into a dense cone-type shell (e.g., Wilkin 1996).

One type of bow shock is known to be associated with pulsars. Having space velocities of $\geq 100 \text{ km s}^{-1}$ (e.g., Hobbs et al. 2005) and strong winds (which carry much of the spin-down energy \dot{E} of pulsars), pulsars moving in the ISM are candidates to drive bow shocks. Thus

far, six pulsars have been found to have a typical bow shock, revealed by the shocks' optical Balmer line emission (Gaensler & Slane 2006). The detected line nebulae are understood to arise from de-excitations of neutral H atoms in the shocked ambient gas, following the processes of collisional excitation or charge-exchange (e.g., Bucciantini & Bandiera 2001). In addition, a pulsar bow shock may also be revealed by the detection of a termination shock of the pulsar wind. The termination shock lies inside a bow shock, and can appear bright at X-ray or radio energies due to synchrotron radiation (Kaspi et al. 2006; Gaensler & Slane 2006).

In our *Spitzer* Infrared Array Camera (IRAC) survey of 7 relatively young pulsars, for the purpose of probing the general existence of debris disks around isolated neutron stars (Wang et al. 2013, in preparation), a mid-infrared (MIR) cometary nebula was serendipitously detected near one of the pulsars, PSR J1549–4848 (hereafter J1549). Naively thinking that the MIR structure is associated with the pulsar, we would have found the first MIR bow shock that arises from the interaction between the pulsar wind and ISM. We thus made follow-up 24 and 70 μm imaging and 7.5–14.4 μm spectroscopic observations with *Spitzer* and optical observations with the Magellan telescopes after the initial detection of the nebula at 8.0 μm . However, our detailed data analyses raise questions about the association between the cometary nebula and the pulsar. On the basis of our observational results, the origin of the nebula is not certain. Here we report our multi-wavelength observations, data analyses, and results. The observations and data reduction are described in § 2, and the data analyses and results are presented in § 3 and § 4, respectively. We discuss the possible origin of the cometary nebula in § 5 and summarize the results in § 6.

¹ Shanghai Astronomical Observatory, Chinese Academy of Sciences, 80 Nandan Road, Shanghai 200030, China

² Physics Department, University of Wisconsin-Milwaukee, Milwaukee, WI 53211, USA

³ Harvard-Smithsonian Center for Astrophysics, 60 Garden Street, Cambridge, MA 02138, USA

⁴ Las Campanas Observatory, Observatories of the Carnegie Institution of Washington, La Serena, Chile

⁵ Department of Physics, McGill University, 3600 University Street, Montreal, QC H3A 2T8, Canada

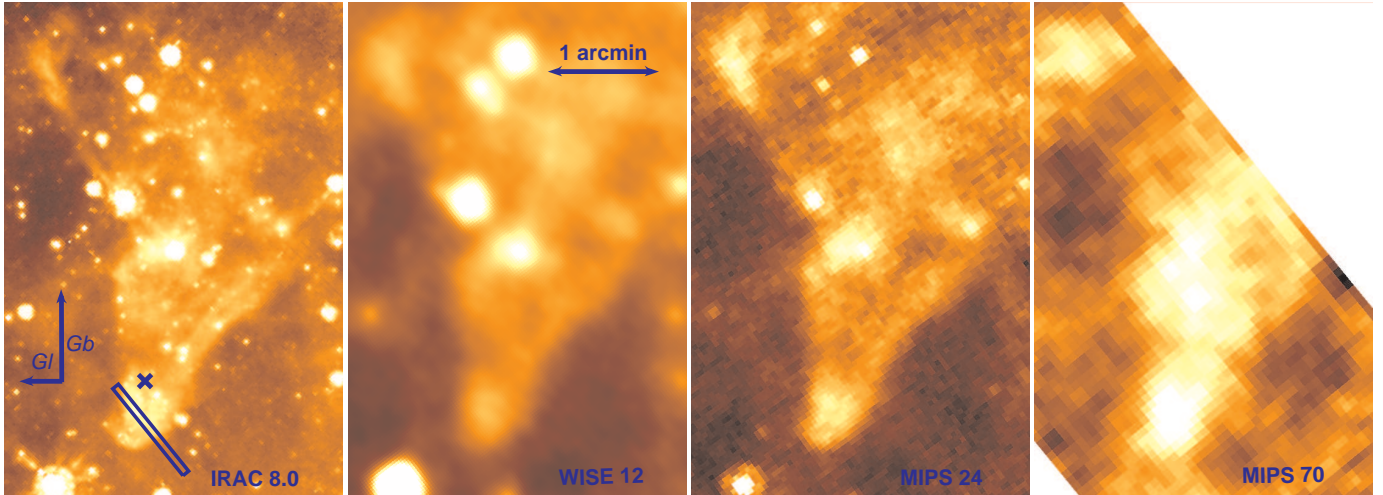


FIG. 1.— *Spitzer* IRAC 8.0 μm (left panel) and MIPS 24 (third panel) and 70 μm (right panel) imaging of the cometary nebula. The WISE third-band 12 μm detection of the nebula is shown in the second panel. In the left panel, the position of J1549 is marked by a cross sign, and one nod position of the slit (which has a size of $57'' \times 3.7''$) in our *Spitzer* IRS observations is indicated with a box region.

2. OBSERVATIONS AND DATA REDUCTION

Our *Spitzer* and ground-based observations of the cometary nebula are summarized in Table 1. Below we describe them and the related data reductions.

2.1. *Spitzer* Imaging

2.1.1. IRAC And MIPS Imaging

As part of our survey program, the initial *Spitzer* observations of J1549 were carried out on 2007 September 12. The imaging instrument used was the Infrared Array Camera (IRAC; Fazio et al. 2004). The field of our target was imaged in the pair of 4.5 and 8.0 μm channels of the IRAC simultaneously. The detectors at the short and long wavelengths were InSb and Si:As devices, respectively, with 256×256 pixels and a plate scale of $1.2''/\text{pixel}$. The field of view (FOV) was $5.2' \times 5.2'$. The frame time was 30 s, with 26.8 effective exposure time per frame. The total exposure time at each channel was 17.87 min. A cometary nebula was detected in the 8.0 μm image (Figure 1) around J1549, but not in the 4.5 μm image.

To study the nebula and derive its properties, we requested *Spitzer* observations at the longer wavelengths. Using Multiband Imaging Photometer for *Spitzer* (MIPS; Rieke et al. 2004), 24 and 70 μm broad-band imaging of the source field was carried out on 2008 August 30. The 24 μm detector was a 128×128 pixel Si:As array, with a pixel size of $2.55''$ and a $5.4' \times 5.4'$ FOV. The 70 μm detector was a 32×32 pixel Ge:Ga array. We chose its wide FOV observing mode for imaging, which provided a pixel scale of $9.85'' \times 10.06''$ and a $5.2' \times 2.6'$ FOV. At 24 and 70 μm , the exposure times were 11.8 and 10.5 min, respectively (frame times $\simeq 3$ sec).

2.1.2. Data Reduction

We started with the Basic Calibrated Data (BCD), provided by *Spitzer* Science Center (SSC). The data were produced from raw images through the IRAC and MIPS data pipelines (IRAC software version was S16.1.10 and MIPS software version was S18.1.0) in SSC. The detailed reduction in the pipelines can be found in the IRAC Data

Handbook (version 3.0) and MIPS data Handbook (version 3.3.1).

For IRAC data, we first used the IRAC artifact mitigation program, distributed as Contributed Software by SSC, to clean the BCD images. Several bright stars in the target field caused column pull-down, row pull-up, or optical banding artifacts. We then corrected each BCD image for array location dependence, using the array location correction images provided by SSC. To combine BCD images into a final post-BCD (PBCD) mosaic at each channel, we used MOPEX, an SSC's package for reducing and analyzing imaging data.

For MIPS 24 μm data, the BCD images do not have any artifacts that need corrections. We used MOPEX to combine the BCD images into a final PBCD mosaic. The MIPS 70 μm BCD images contain horizontal and vertical strips, which were due to response variations and stim latents (stims were MIPS's built-in calibration light sources, which flashed during an observation sequence; for details, see MIPS Data Handbook), respectively. We used the GeRT package, which is provided for MIPS 70 & 160 μm data reductions, to clean up the BCD images. During the reduction, the region that contains our source was masked out. The BCD images were combined into one final PBCD mosaic using MOPEX.

2.2. *Spitzer* Spectroscopy

2.2.1. IRS Observations

Our *Spitzer* spectroscopic observations were made on 2009 September 14. The instrument was the Infrared Spectrograph (IRS; Houck et al. 2004). We used the Short-Low (SL) module of the IRS for the observations, which provided a wavelength coverage of 7.5–14.4 μm (first order) and a resolving power of 61–120. The detector was a 128×128 arsenic doped silicon (Si:As) array, with a pixel scale of $1.8''/\text{pixel}$. The slit in the first order had a length \times width of $57'' \times 3.7''$. We obtained a set of 16 spectra at each of two default nod positions along the slit. The integration time for each individual spectrum was 60.95 s, and the total on-source time was 32.5 min. In addition, since our target is an extended source, we

used the exact same observing mode and obtained spectra of a nearby sky region for background subtraction.

2.2.2. Data Reduction

We started with the BCD images, produced from the SSC IRSX Channel-0 Software (version S18.7.0). We first combined all the sky BCD images into one master sky image and subtracted this master image from each of the target BCD images. We then used the `IRSCLEAN_MASK` program, provided by SSC, to construct a super mask by combining the rogue pixel mask for the campaign IRSX009500 (in which our IRS observations were made) and additional bad pixels identified by `IRSCLEAN_MASK`. The super mask was used in the `IRSCLEAN` program for cleaning up bad pixels in the BCD images. The BCD images were combined into one final image by using the `coa2d.pro` program.

We used `SPICE`, an IRS spectrum extraction software provided by SSC, to extract the spectrum of the nebula. The width of the extraction box was 15 pixels ($27''$), which covers the 2-D spectrum image well. The spectra at two nod positions were extracted and average-combined into the final source spectrum.

2.3. WISE Imaging

Launched on 2009 December 14, the Wide-field Infrared Survey Explorer (WISE) mapped the entire sky at 3.4, 4.6, 12, and 22 μm (called W1, W2, W3, and W4 bands, respectively) in 2010 with FWHMs of $6.1''$, $6.4''$, $6.5''$, and $12.0''$ in the four bands, respectively (see Wright et al. 2010 for details). The WISE all-sky images and source catalogue were released in 2012 March. We downloaded the WISE image data of the source field from the Infrared Processing and Analysis Center (IPAC), and found that the cometary nebula was detected in the W3 and W4 bands but not in the first two bands. The WISE observations were made between 2010 Feb. 22-25 and the depth of coverage was ~ 13.7 pixels (corresponding to 110 s on-source integration time).

2.4. Ground-Based Observations

2.4.1. Optical/Near-Infrared Imaging

We also observed the target field in R broad band and H_α narrow band on 2008 June 15, using Inamori-Magellan Areal Camera and Spectrograph (IMACS) on the 6.5-m Baade Magellan Telescope at Las Campanas Observatory in Chile. The long camera (known as f/4) of IMACS was used. The detector of the camera consists of 8 2048×4096 pixel² SITE ST-002A CCDs. Under the f/4 imaging mode, the camera provides a field coverage of 15.4×15.4 and a pixel scale of $0''.111$ pixel⁻¹. The exposure times of the images were 4 min in R and 18.3 min in H_α . The observing conditions were good, with seeing being $0''.65$. In addition, we observed standard stars PG1633+099 (Landolt 1992) in R band and LTT7379 (Hamuy et al. 1994) in H_α for flux calibration.

We included near-infrared (NIR) K_s imaging data of the target field, obtained on 2006 May 17 as part of our IR survey of a few young pulsars (like J1549). The observation was also made with the Baade Magellan Telescope. The NIR camera was Persson's Auxiliary Nasmyth Infrared Camera (PANIC; Martini et al. 2004). The

detector was a Rockwell Hawaii 1024×1024 HgCdTe array, having a field of view (FOV) of $2' \times 2'$ and a pixel scale of $0''.125$ pixel⁻¹. The total on-source exposure time was 22.5 min. During the exposure, the telescope was dithered in a 3×3 grid with offsets of $10''$ to obtain a measurement of the sky background. The observing conditions were good, with $0''.4$ seeing in K_s .

2.4.2. Data Reduction

We used the IRAF data analysis package for data reduction. The images were bias-subtracted and flat-fielded. In addition for the NIR data, a sky image was made by filtering out stars from each set of dithered images in one observation. The sky image was subtracted from the set of images, and then the sky-subtracted images were shifted and combined into one final image of the target field.

3. ANALYSIS

3.1. Astrometry

The pointing of the IRAC frames is typically accurate to $0''.5$. In order to determine more accurately the position of the cometary nebula and locate J1549 on the images, we astrometrically calibrated the IRAC 8.0 μm image by matching stars detected in this image to Two Micron All-Sky Survey (2MASS; Skrutskie et al. 2006) stars. For this calibration, 190 2MASS stars were used. The nominal uncertainty of the calibrated image is dominated by the 2MASS systematic uncertainty ($\simeq 0''.15$, with respect to the International Celestial Reference System). The other images were also positionally calibrated by matching them to the 8.0 μm image.

3.2. Morphology

We studied the cometary structure by semi-quantitatively determining its shape. The 8.0 μm image was used for the detailed study because it has the best resolution among the *Spitzer* and WISE detections. We first removed all point sources near the cometary structure. Using the software package `APEX` (multi-frame extraction) provided by SSC, point sources in the field were identified and subtracted from each BCD image. The residual frames were then combined into a PBCD mosaic, which is shown in Figure 2.

We then manually selected small regions along the three parts of the nebula: the two wings and the head region. Narrow box regions set parallel to the three nebula parts were defined, with each box having a length \times width of 5×1 pixel² ($6''.1 \times 1''.2$). Photons within each box were counted and the uncertainty on the photon counts was estimated as the square-root of the total counts. This way a brightness curve that was perpendicular to the narrow box regions (or to the nebula parts) was obtained. Using a Gaussian function, we performed least-squares fitting to the brightness curve and thus determined the location of a brightness peak point. The uncertainty for each location was also estimated from the fitting. In total 19 such brightness peak points were determined (see Figure 2).

3.3. Photometry

We obtained the flux of the head region of the cometary nebula at each band. A circular region with a radius of $21''$, which well covers the head region, was used as the

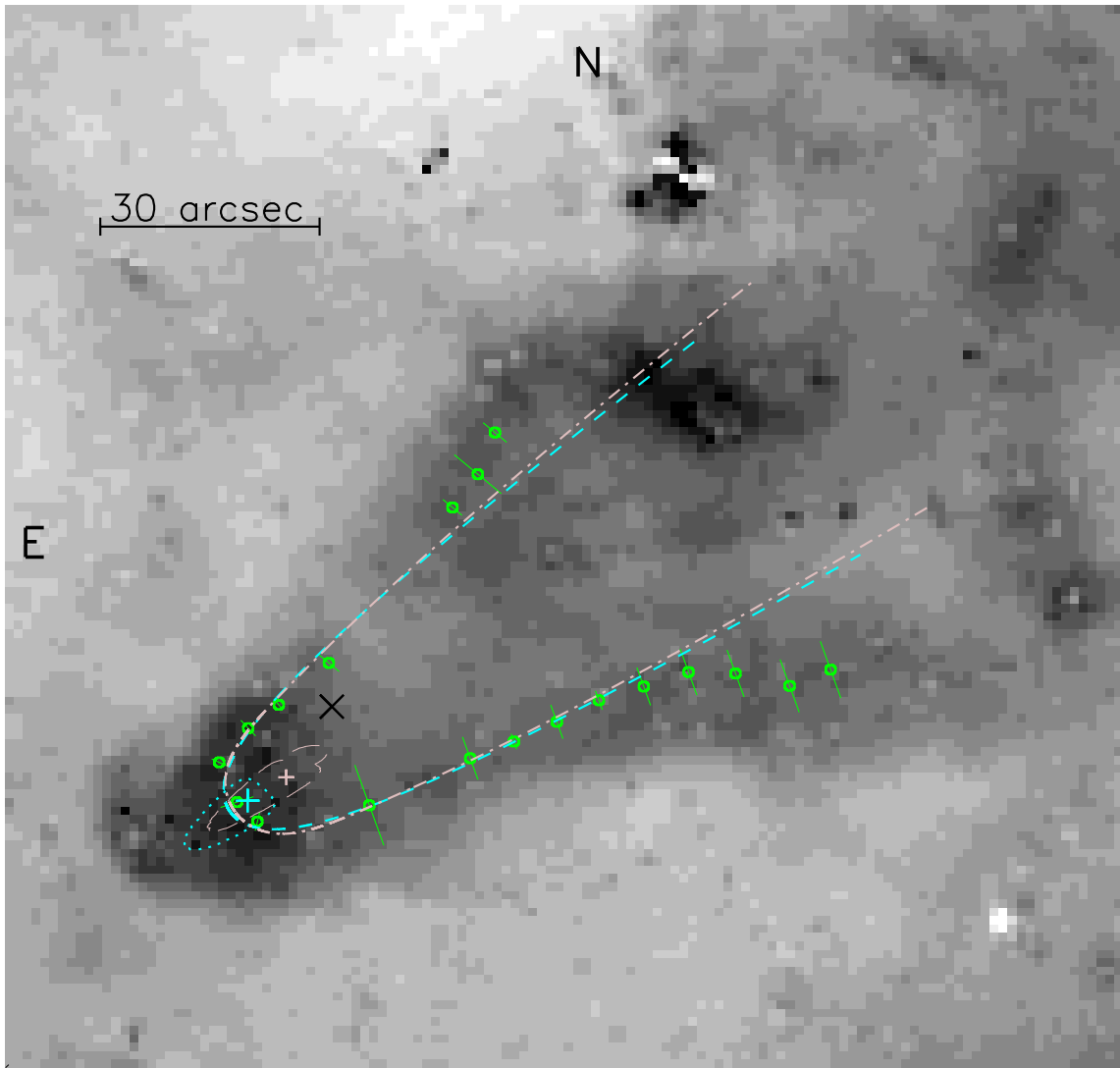


FIG. 2.— *Spitzer* IRAC 8.0 μm PBCD image of the cometary nebula with in-field stars removed. The small circles mark the brightness peak points we obtained for the nebula (see Section 3.2). The position of the pulsar J1549 is marked by a black cross sign. The dotted curve indicates the 3σ region in which the associated object is considered to be located (obtained from fitting the analytic solution for bow shocks provided by Wilkin 1996), with the large plus sign marking the best-fit position and dashed curve being the best-fit. The long dashed curve indicate the same region obtained from fitting the analytic solution for pulsar bow shocks provided by Vigelius et al. (2007), with the small plus sign marking the best-fit position and dot-dashed curve being the best-fit.

photometry aperture. A box region of $80'' \times 50''$ near the head was used for estimating the sky background brightness. For photometry at 8.0 μm , aperture correction was required because IRAC imaging uses point sources for flux calibration. We used the function form provided by SSC to calculate the correction factor and found a value of 0.83 for a radius of $21''$. The flux value at 8.0 μm is the measured flux value times the correction factor. We also derived the flux upper limit for the 4.5 μm non-detection, because the deep image provides an additional constraint on MIR emission from the cometary nebula.

Following the guidelines given for aperture photometry on the WISE atlas images⁶, WISE W3 and W4 fluxes were also obtained. The broad-band flux measurements and 4.5 μm upper limit are given in Table 1.

4. RESULT

4.1. Location of the Associated Object

The shape of the IR cometary nebula indicates that it is likely a typical bow shock. The location of the associated object that drives the IR nebula can thus be estimated by fitting the nebula with a standard bow-shock shape, since the distance from an associated object to the apex of the associated bow shock (so-called “stand-off distance”) sets the length scale of the bow shock. We considered an analytic solution derived by Wilkin (1996), $r_\theta \sin \theta = r_a \sqrt{3(1 - \theta/\tan \theta)}$, where r_θ is the distance between the bow shock shell and the associated object, θ is the polar angle from the axis of symmetry (i.e., the associated object’s moving direction), and r_a is the standoff distance. With this solution, we fit the positions of the brightness peak points obtained in § 3.2. The free parameters in the fitting were x , y location of the associated object, r_a , and the rotation angle of the axis of the bow

⁶ http://wise2.ipac.caltech.edu/docs/release/allsky/expsup/sec2_3f.html

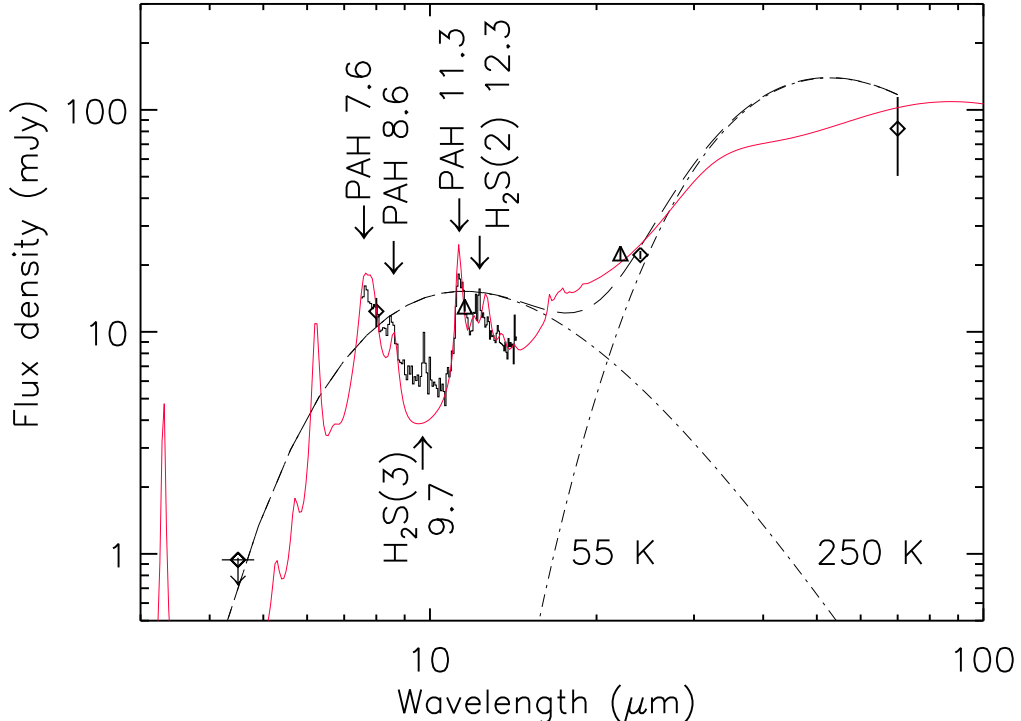


FIG. 3.— Dereddened spectrum of the head region of the cometary nebula, which consists of the *Spitzer* broad-band 4.5 μm flux upper limit, 8.0, 24, and 70 μm fluxes (diamonds) and IRS 7.5–14.4 μm spectrum (solid histogram), and WISE 12 and 22 μm fluxes (triangles). Dust emission from two temperature components (250 K and 55 K, both dot-dashed curves; their sum, long-dashed curve) can generally describe the spectrum. The model spectrum of irradiated dust emission given by Draine & Li (2007) is plotted as the red solid curve.

shock in the plane of the sky. To simplify the fitting, we assumed that the axis of symmetry of the bow shock lies nearly in the plane of the sky (note that an inclination angle such as 60° will result in a smaller projected distance between the associated object and the ‘apparent’ apex of the bow shock).

The obtained (3σ) region in which the associated object is located is indicated as a dotted contour in Figure 2. It is a small region very close to the head of the cometary nebula, and approximately $15''$ away from J1549 (whose position is R.A. = $15^{\text{h}}49^{\text{m}}21^{\text{s}}.15$, Decl. = $-48^\circ48'37''.4$, equinox J2000.0, and has an uncertainty of $\approx 1''$; D’Amico et al. 1998). Because the data points of the brightness peaks do not provide tight constraints along the axis of symmetry, the region is more extended along this direction. The best-fit location and bow shock solution are shown as a plus sign and a dashed curve, respectively, in Figure 2. As can be seen, the standard bow shock shape generally fits the data points, although the tail of the nebula is wider, deviating away from the model. From the best fit ($\chi^2=14$ for 15 degrees of freedom), we found $r_a \approx 2''.9$.

4.2. Mid-IR Spectrum

In Figure 3, we show the broad-band and *Spitzer* IRS spectrum of the head region of the cometary nebula, which is dereddened with $E(B-V) = 1.1$ (Schlegel et al. 1998) using the interstellar extinction laws given by Indebetouw et al. (2005) for wavelengths $\leq 8 \mu\text{m}$ and by Weingartner & Draine (2001) for wavelengths $> 8 \mu\text{m}$. The *Spitzer*/IRAC 4.5 μm flux upper limit is also in-

cluded. The IRS spectrum was flux calibrated by equaling the average value of its 7.5–8.5 μm region to the IRAC 8.0 μm broad-band flux value. A few emission lines were detected in the IRS spectrum, which are polycyclic aromatic hydrocarbon (PAH) 11.3, 8.6, and likely 7.6 μm . These PAH lines are commonly seen in many emission nebulae and arise from vibrational modes of PAH in dust (e.g., Draine 2003). Two H_2 rotational lines were also detected, although weakly. They are $\text{H}_2\text{S}(3)$ 9.7 μm and $\text{H}_2\text{S}(2)$ 12.3 μm . In general, H_2 lines are associated with photodissociation regions (PDRs; e.g., Hollenbach & Tielens 1997) or shock interaction regions (e.g., Shinn et al. 2009). We note that the broad dip at $\sim 9.7 \mu\text{m}$ is not the well-known silicate absorption feature. Rather, its appearance is caused by the nearby strong PAH emission features (Draine & Li 2007). The total Galactic reddening along the line of sight to the source is only approximately $E(B-V) = 1.1$ (for $l=330^\circ.5$, $b=4^\circ.3$; Schlegel et al. 1998). If the dip is caused by interstellar reddening, $E(B-V)$ should be ≥ 4 , which is too large to be consistent with those estimated from the all-sky dust (Schlegel et al. 1998) or neutral hydrogen density (Dickey & Lockman 1990) maps. Also, as shown below in this section, the local column density of the cometary nebula is much lower than that implied by the reddening $E(B-V) \geq 4$.

We first tested using a simple dust grain model (Dwek & Werner 1981) to reproduce the spectrum we obtained. This model was developed to explain the observed IR emission from supernova remnants (SNRs), in which dust grains are heated both by collisions with am-

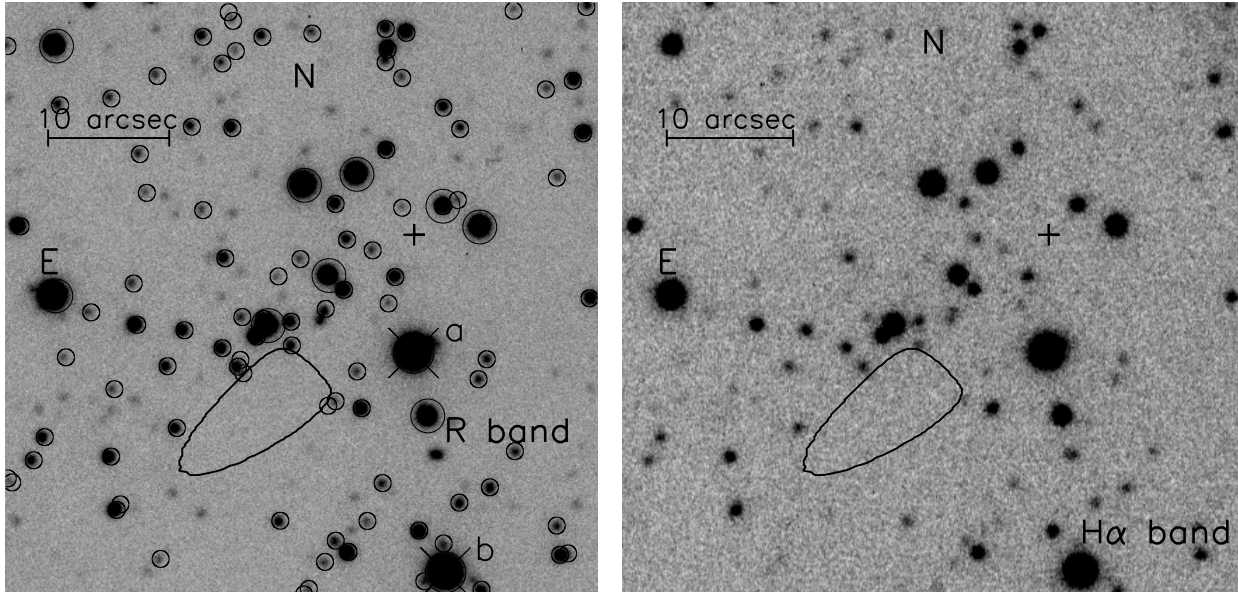


FIG. 4.— Optical R (left panel) and $H\alpha$ (right panel) images of the field of the IR cometary nebula. In each panel, the region in which the associated source should be located is indicated by the solid curve, while the position of J1549 is indicated by the plus sign. Photometry of the field stars (marked by circles in the left panel) was performed, and star a and b (marked by cross signs) was slightly saturated in the R and K_s image, respectively.

bient thermal gas and by radiation flux, and could work for the IR nebula in our case. Considering the general case that the grains' absorption/emission efficiency decreases as λ^{-2} , we found that two components with temperatures of $T_h = 250$ K and $T_l = 55$ K (assuming a simplified, uniform grain size of radius $0.1 \mu\text{m}$), can generally describe the spectrum (Figure 3). The dust masses thus simply estimated are $1.0 \times 10^{25} d_{\text{kpc}}^2$ g and $1.9 \times 10^{29} d_{\text{kpc}}^2$ g, respectively, where d_{kpc} is the source distance in units of kpc.

To better reproduce the IRS spectrum, a detailed model including PAH particles is needed. We considered the model spectra derived and provided by Draine & Li (2007), although we note that in their model, dust grains are heated by a field of starlight. According to their calculations, for the case of dust grains being heated by a single radiation intensity, the flux ratio between 24 and $70 \mu\text{m}$ is mainly sensitive to radiation with energy density per unit frequency UU_{ISRF} , where U_{ISRF} is the interstellar radiation field (ISRF) estimated by Mathis et al. (1983) for the solar neighborhood and U is a dimensionless scaling factor. We thus found that $U = 0.1$ is required for our data points. However, the $U = 0.1$ model spectra have much stronger PAH features than those in our IRS spectrum (even with the lowest PAH mass fraction $q_{\text{PAH}} = 0.47\%$; $q_{\text{PAH}} \simeq 4.6\%$ is found to be applicable to the dust in the Milky Way). In order to have a good fit to the IRS spectrum, we found that the dust should be heated by a single radiation intensity, $U = 12$, plus by a power-law distribution of starlight intensities ranging from $U = 12$ – 10^6 (where $q_{\text{PAH}} \simeq 4.6\%$, the power-law index α is fixed, $\alpha = -2$, and the fraction of the dust mass that is exposed to the distribution of starlight intensities is $\gamma = 0.16$; cf. equation (23) in Draine & Li 2007). This model spectrum is displayed in

Figure 3, which generally describes the PAH features in our spectrum. As a result, the dust mass M_{dust} can be estimated from the total value of the 24, 70, and $160 \mu\text{m}$ fluxes (cf. equation (34) in Draine & Li 2007). Since no flux measurement at $160 \mu\text{m}$ was obtained, M_{dust} should be $\geq 1.2 \times 10^{29} d_{\text{kpc}}^2$ g and $\simeq 1.9 \times 10^{29} d_{\text{kpc}}^2$ g when assuming the flux at $160 \mu\text{m}$ is equal to that at $70 \mu\text{m}$. The value range is consistent with that derived above from the simple dust grain model.

We further estimated the properties of the head region of the bow shock. Considering again the dust size of $0.1 \mu\text{m}$ (and density of 3 g cm^{-3} ; Dwek & Werner 1981), the total luminosities in the region were $5.7 \times 10^{31} d_{\text{kpc}}^2$ and $1.1 \times 10^{32} d_{\text{kpc}}^2 \text{ erg s}^{-1}$ for the 250 K and 55 K dust grains, respectively. Simply assuming that the head region is a $21''$ radius (or $0.1 d_{\text{kpc}}$ pc) sphere, the number density (dominated by the cold dust grains) can be estimated to be $\sim 90 \text{ cm}^{-3}$, where a mass ratio of 1 to 100 between the dust to gas is used (Draine et al. 2007).

4.3. $H\alpha$ Non-Detection

In order to search for possible line emission from the bow shock, we made both R and $H\alpha$ imaging observations of the target field with the Magellan telescopes; the wide-band image was used to serve as the continuum flux. We did not detect any $H\alpha$ nebula in our observations. Both optical R - and $H\alpha$ -band images of the target field are shown in Figure 4. The R -band detection limit was ~ 23 mag, and the $H\alpha$ flux upper limit (3σ) was $2.9 \times 10^{-14} \text{ erg s}^{-1} \text{ cm}^{-2} \text{ arcsec}^{-2}$.

5. DISCUSSION

Provided with the results we have obtained from the above analyses, we discuss the possible origin of this bow

shock by first considering a stellar object and then J1549 as the associated star.

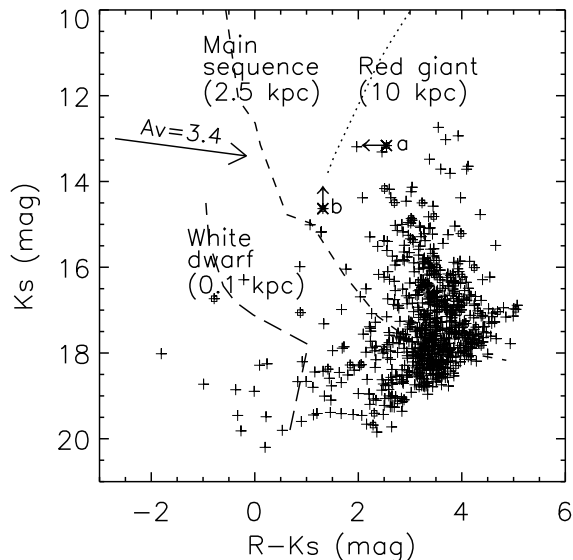


FIG. 5.— K_s versus $R - K_s$ diagram of the in-field stars near the bow shock. Data points marked by squares are those stars highlighted by circles in the left panel of Figure 4. The total Galactic extinction of $A_V = 3.4$ is indicated by the arrow. The two stars marked with arrows are those two nearby stars slightly saturated in our R or K_s images (Figure 4), with the arrows indicating their magnitude or color limit. Color-magnitude curves for main-sequence stars, red giants, and white dwarfs are plotted as the dashed, dotted, and long-dashed lines.

5.1. A Stellar Bow Shock?

As shown by our analysis in § 4.1, considering an isotropic wind/outflow from an object (Wilkin 1996), the location of the associated object would likely be within a small area near the head region of the bow shock, which is more than $15''$ away from PSR J1549. Such IR bow shocks can be driven by either massive stars with a strong wind (van Buren et al. 1990; Peri et al. 2012) or giant stars ejecting mass (Martin et al. 2007; Cox et al. 2012), as long as the associated stars are moving supersonically in the ISM. The stand-off distance of such a bow shock is given by $r_a = (\dot{m}_w V_w / 4\pi\rho V_*^2)^{1/2}$ (e.g., Wilkin 1996), where \dot{m}_w is the mass loss rate, V_w is the wind velocity, and ρ is the density of the ISM. For a massive O/B star with typical values of $\dot{m}_w = 10^{-7} M_\odot \text{ yr}^{-1}$, $V_w = 1000 \text{ km s}^{-1}$, and $V_* = 30 \text{ km s}^{-1}$ (see, e.g., Peri et al. 2012), the required ambient ISM hydrogen density to produce the observed bow shock is $n_H \simeq 1500(\dot{m}_{w-7} V_{w3} / V_{*30}^2 d_{\text{kpc}}^2) \text{ cm}^{-3}$, where \dot{m}_{w-7} is the mass loss rate in units of $10^{-7} M_\odot \text{ yr}^{-1}$, V_{w3} is the wind velocity in units of 1000 km s^{-1} , and V_{*30} is the star’s space velocity in units of 30 km s^{-1} . Here we have used $r_a = 2.9d = 4 \times 10^{16} d_{\text{kpc}} \text{ cm}$ and $\rho = \mu m_H n_H$ with $\mu_H = 1.4$ (μ_H is the mean nucleus number per hydrogen atom and m_H is the mass of the hydrogen nucleus). Using the low end value of $\dot{m}_{w-7} = 0.1$ and $d_{\text{kpc}} = 10$ (see below for a discussion of the distance), along with the other mass-loss parameters given above, we find $n_H \approx 1$, broadly consistent with values expected for the ISM density. Alternatively, for a giant star with mass ejection, $V_w \simeq 10 \text{ km s}^{-1}$ and other parameters similar to those

above (e.g., Cox et al. 2012), the required ambient density is $n_H \simeq 15$; reasonable adjustments to the parameters can easily lead to values more consistent with the ISM density. These calculations thus show that it is possible to have either a massive star or a giant star with mass ejection as the object that drives the bow shock.

However we evaluated the possible association of the bow shock with any in-field stars and obtained negative results. First there were no stars detected in the associated object region in our optical images down to $R \simeq 23$ (see Figure 4). We also analyzed the nearby stars by constructing a color-magnitude diagram of K_s versus $R - K_s$ (Figure 5). As can be seen, the stars are consistent with being low-mass main sequence stars (or white dwarfs) at distances of $\lesssim 2.5 \text{ kpc}$. Massive or giant stars would have to be at distances of $\sim 6 \text{ kpc}$ and $\sim 10 \text{ kpc}$, respectively, and approximately $0.5\text{--}0.8 \text{ kpc}$ away from the Galactic plane, a place not likely to form bow shocks due to the low density of the ISM. The detection of H_2 lines in the IRS spectrum suggests that the associated object should probably be $\lesssim 0.1 \text{ kpc}$ away from the Galactic plane, since molecular gas generally inhabits within the mid-plane of the Galactic disk (Cox 2005).

5.2. PSR J1549 as the Associated Object?

Given their high space velocities ($\geq 100 \text{ km s}^{-1}$) and strong winds, pulsars can naturally drive bow shocks in the ISM. Detections of bow shocks around pulsars at multiple wavelength ranges have provided sufficient evidence for it (Kaspi et al. 2006; Gaensler & Slane 2006). The existence of IR bow shocks, arising due to irradiation or collisional heating, can be expected. The pulsar J1549 has a spin-down energy of $\dot{E} = 2.3 \times 10^{34} \text{ erg s}^{-1}$ and a distance of 1.5 kpc (D’Amico et al. 1998), implying that if it were associated with the bow shock, approximately 1.6% of the energy is used to illuminate the dust, which is a reasonable fraction to consider (note the total luminosity from the head of the bow shock is $\sim 3.8 \times 10^{32} \text{ erg s}^{-1}$ at the distance of 1.5 kpc). On the other hand, the pulsar’s kinematic energy can also contribute to dust heating. Considering a radius $r = 0.15 \text{ pc}$ (the head region we have defined when the distance is 1.5 kpc) interaction area, the energy received by the ambient medium is $(1/2\rho V^2) \cdot V \cdot (\pi r^2) \approx 6.4 \times 10^{33} n_H V_{200}^3 \text{ erg s}^{-1}$, where $n_H \simeq 1 \text{ cm}^{-3}$ and $V = 200 \text{ km s}^{-1}$, the pulsar’s velocity, are used. Therefore there is sufficient energy to illuminate the bow shock.

The obvious challenge to this interpretation is J1549’s location, which is at least $15''$ (or 0.11 pc if at the pulsar’s distance) away from the determined area for the associated object of the bow shock. However, we note that a pulsar wind can be highly anisotropic and for peculiar cases, long jet-like outflows have been detected from pulsars (Johnson & Wang 2010; De Luca et al. 2011). Calculations for such anisotropic wind cases to produce bow shocks have been considered (e.g., Wilkin 2000). One feature that has been revealed is the off-axis location of an associated star if the star’s wind points away from the direction of the stellar motion, for which the star’s location would otherwise be determined to lie in the apparent axis of symmetry when simply fitting the stand-off region (Wilkin 2000). Vigelius et al. (2007) did further detailed simulations by considering the anisotropy of pulsar winds

for pulsar bow shocks, and have shown that a variety of shape changes with respect to the ‘standard’ shape of bow shocks. In particular, the broadening of the tails of the bow shocks in their simulations SA and SB (see Figure 13 in their paper), when a pulsar runs through a wall of the high-density ISM with finite width, is possibly observed in our case (see Figure 2). We thus did test fitting to our cometary nebula by using equation A11 given in Vigelius et al. (2007), an analytic solution for jet-like outflows (λ , c_0 , and c_2 were simply set to be 0, 0, and 5, where λ sets the angle between the directions of the pulsar’s wind and its motion; for details see Vigelius et al. 2007). The best-fit solution ($\chi^2 = 13$ for 15 degrees of freedom) is shown in Figure 2, which is nearly the same as that found in Section 4.1. The allowed 3σ region for the associated object is however substantially elongated toward J1549. While the pulsar is still $5.8''$ away from the region, the fitting results suggest that it may be possible for the pulsar to drive the bow shock if it had a highly-collimated wind and the wind were tilted away from the direction of the pulsar’s motion. In order to fully explore this possibility, detailed hydrodynamic simulations, such as those carried out by Vigelius et al. (2007), are needed.

In addition, if J1549 did have a highly collimated pulsar wind, the interaction of its wind with the ambient medium could be detectable at X-ray energies. X-ray imaging should be carried out to search for the interaction, which would lie from J1549 to the stand-off region of the IR nebula, thus verifying the association of the pulsar with the nebula. The bow shock has a direction towards the Galactic plane (Figure 1), implying that the associated object is moving in the same direction. High-spatial resolution radio imaging of the pulsar, to detect its proper motion, should also be carried out. If J1549 is also moving in this direction, its chance of being associated with the bow shock would be substantially increased.

6. SUMMARY

We have discovered an IR bow shock around the pulsar J1549, and from our follow-up imaging and spectroscopic observations and WISE all-sky survey data, a composite spectrum of its head region from 8 to $70 \mu\text{m}$, which includes a *Spitzer* IRS 7.5– $14.4 \mu\text{m}$ spectrum, was obtained. In the IRS spectrum, a few PAH and H_2 emission features were detected. Considering the overall spectrum with these features, the emission likely arises from the

dust grains in the interaction region heated by collisions and/or radiation flux from the associated object. The dust mass in the region was estimated to be 2×10^{29} g. We analyzed the shape of the bow shock by fitting with a standard analytic solution for such objects, and the derived region in which the associated object would be located is $15''$ away from J1549. This raises the question of which object drives this bow shock. No stars were detected in the associated object region down to $R \sim 23$, and moreover our studies of the in-field stars indicate that none of them are likely bright O/B stars or red giants located near the Galactic plane, which are able to drive such bow shocks due to their strong winds or mass ejection. Given the considered properties of pulsar winds, including a few peculiar pulsar jet-like outflows, we suggest that it is possible for J1549 to be associated with the IR bow shock if it had a highly collimated wind. Hydrodynamic simulations of the interaction of such a wind with the ISM can help explore this possibility. In addition, X-ray imaging to detect the interaction of its wind with the ambient medium and high-spatial resolution radio imaging to detect the proper motion of the pulsar will help verify their association.

This work is based in part on observations made with the *Spitzer* Space Telescope, which is operated by the Jet Propulsion Laboratory, California Institute of Technology under a contract with NASA. The publication makes use of data products from the Wide-field Infrared Survey Explorer, which is a joint project of the University of California, Los Angeles, and the Jet Propulsion Laboratory/California Institute of Technology, funded by NASA.

This research was supported by National Basic Research Program of China (973 Project 2009CB824800), and National Natural Science Foundation of China (11073042). ZW is a Research Fellow of the One-Hundred-Talents project of Chinese Academy of Sciences. PS acknowledges partial support from NASA Contract NAS8-03060. VMK holds a Canada Research Chair and the Lorne Trottier Chair in Astrophysics & Cosmology, and is a Fellow of the Royal Society of Canada.

Facilities: Magellan (PANIC, IMACS), *Spitzer* (IRAC, IRS)

REFERENCES

- Bucciantini, N., & Bandiera, R. 2001, *A&A*, 375, 1032
 Cox, D. P. 2005, *ARA&A*, 43, 337
 Cox, N. L. J., et al. 2012, *A&A*, 537, A35
 D’Amico, N., et al. 1998, *MNRAS*, 297, 28
 De Luca, A., et al. 2011, *ApJ*, 733, 104
 Dickey, J. M., & Lockman, F. J. 1990, *ARA&A*, 28, 215
 Draine, B. T. 2003, *ARA&A*, 41, 241
 Draine, B. T., & Li, A. 2007, *ApJ*, 657, 810
 Draine, B. T., et al. 2007, *ApJ*, 663, 866
 Dwek, E., & Werner, M. W. 1981, *ApJ*, 248, 138
 Fazio, G. G., et al. 2004, *ApJS*, 154, 10
 Gaensler, B. M., & Slane, P. O. 2006, *ARA&A*, 44, 17
 Hamuy, M., Suntzeff, N. B., Heathcote, S. R., Walker, A. R., Gigoux, P., & Phillips, M. M. 1994, *PASP*, 106, 566
 Hobbs, G., et al. 2005, *MNRAS*, 360, 974
 Hollenbach, D. J., & Tielens, A. G. G. M. 1997, *ARA&A*, 35, 179
 Houck, J. R., et al. 2004, *ApJS*, 154, 18
 Indebetouw, R., et al. 2005, *ApJ*, 619, 931
 Johnson, S. P., & Wang, Q. D. 2010, *MNRAS*, 408, 1216
 Kaspi, V. M., Roberts, M. S. E., & Harding, A. K. 2006, in *Compact stellar X-ray sources*, ed. W. H. G. Lewin & M. van der Klis, 279–339
 Landolt, A. U. 1992, *AJ*, 104, 340
 Martin, D. C., et al. 2007, *Nature*, 448, 780
 Martini, P., Persson, S. E., Murphy, D. C., Birk, C., tman, S. A. S., Gunnels, S. M., & Koch, E. 2004, *Proc. SPIE*, 5492, 1653, (astro-ph/0406666)
 Mathis, J. S., Mezger, P. G., & Panagia, N. 1983, *A&A*, 128, 212
 Morton, T. D., et al. 2007, *ApJ*, 667, 219
 Peri, C. S., Benaglia, P., Brookes, D. P., Stevens, I. R., & Isequilla, N. L. 2012, *A&A*, 538, A108
 Rieke, G. H., et al. 2004, *ApJS*, 154, 25
 Schlegel, D. J., Finkbeiner, D. P., & Davis, M. 1998, *ApJ*, 500, 525

TABLE 1
OBSERVATIONS AND FLUX MEASUREMENTS OF THE COMETARY NEBULA AROUND J1549

Observation date	Telescope/Instrument	Band/Wavelength (μm)	Exposure (min)	Flux measurement (mJy)
2006 May 17	Magellan/PANIC	K_s	22.5	...
2007 Sept 12	Spitzer/IRAC	4.5	26.8	<0.8
		8.0	26.8	10.8 \pm 1.6
2008 June 15	Magellan/IMACS	R	4.0	...
		H_α	18.3 ^a	...
2008 Aug 30	Spitzer/MIPS	24	11.8	20.9 \pm 0.9
		70	10.5	82 \pm 32
2009 Sept 14	Spitzer/IRS	7.5–14.4	32.5	...
2010 Feb 22–25	WISE	3.4	1.8	...
		4.6	1.8	...
		12	1.8	11.4 \pm 0.6
		22	1.8	21.1 \pm 1.6

^a The surface flux upper limit in H_α band is given in § 4.3.

Shinn, J., Koo, B., Burton, M. G., Lee, H., & Moon, D. 2009, ApJ, 693, 1883
 Skrutskie, M. F., et al. 2006, AJ, 131, 1163
 van Buren, D., et al. 1990, ApJ, 353, 570
 Vigelius, M., et al. 2007, MNRAS, 374, 793

Weingartner, J. C., & Draine, B. T. 2001, ApJ, 548, 296
 Wilkin, F. P. 1996, ApJ, 459, L31
 —. 2000, ApJ, 532, 400
 Wright, E. L., et al. 2010, AJ, 140, 1868